J Digit Imaging (2014) 27:520–537
DOI 10.1007/s10278-014-9685-0

Neural Network Ensemble Based CAD System for Focal Liver Lesions from B-Mode Ultrasound

Jitendra Virmani · Vinod Kumar · Naveen Kalra · Niranjan Khandelwal

Published online: 1 April 2014

Abstract A neural network ensemble (NNE) based computer-aided diagnostic (CAD) system to assist radiologists in differential diagnosis between focal liver lesions (FLLs), including (1) typical and atypical cases of Cyst, hemangioma (HEM) and metastatic carcinoma (MET) lesions, (2) small and large hepatocellular carcinoma (HCC) lesions, along with (3) normal (NOR) liver tissue is proposed in the present work. Expert radiologists, visualize the textural characteristics of regions inside and outside the lesions to differentiate between different FLLs, accordingly texture features computed from inside lesion regions of interest (IROIs) and texture ratio features computed from IROIs and surrounding lesion regions of interests (SROIs) are taken as input. Principal component analysis (PCA) is used for reducing the dimensionality of the feature space before classifier design. The first step of classification module consists of a five class PCA-NN based primary classifier which yields probability outputs for five liver image classes. The second step of classification module consists of ten binary PCA-NN based secondary classifiers for NOR/Cyst, NOR/HEM, NOR/HCC, NOR/MET, Cyst/HEM, Cyst/HCC, Cyst/MET, HEM/HCC, HEM/MET and HCC/MET classes. The probability outputs of five class PCA-NN based primary classifier is used to determine the first two most probable classes for a test instance, based on which it is directed to the corresponding binary PCA-NN based secondary classifier for crisp classification between two classes. By including the second step of the classification module, classification accuracy increases from 88.7 % to 95 %. The promising results obtained by the proposed system indicate its usefulness to assist radiologists in differential diagnosis of FLLs.

Keywords Focal liver lesions · B-mode ultrasound · Texture analysis · Neural network ensemble · Computer-aided diagnostic system · Principal component analysis

Glossary

Anechoic FLL	Anechoic focal liver lesion: The focal liver lesion which appears without echoes on ultrasound.
Atypical cyst	Atypical cyst: Appears with irregular, thickened wall and internal echoes.
Atypical FLL	Atypical focal liver lesion: Focal liver lesion with non-specific sonographic appearance.
Atypical HEM	Atypical hemangioma: Appears as isoechoic or even hypoechoic lesion.
Atypical MET	Atypical metastasis: Appearance is extremely variable, ranging from anechoic, hypoechoic, isoechoic, hyperechoic and even with mixed echogenicity.
Benign FLL	Benign focal liver lesion: Non-cancerous focal liver lesion.
B-mode US	B-mode ultrasound: Brightness-mode ultrasound is a two-dimensional representation of echo-producing interfaces in a single plane.
CYST	Liver cyst: Abnormal fluid filled sacs in the liver.

J. Virmani (✉)
Department of Electronics and Communication Engineering, Jaypee University of Information Technology, Waknaghat, Solan, 173234 Himachal Pradesh, India
e-mail: jitendra.virmani@gmail.com

V. Kumar
Department of Electrical Engineering, Indian Institute of Technology-Roorkee, Roorkee, 247667 Uttarakhand, India

N. Kalra · N. Khandelwal
Department of Radiodiagnosis and Imaging, Post-Graduate Institute of Medical Education and Research, Sector-12, Chandigarh, 160012 India

FLL	Focal liver lesion: Focal liver lesion refers to area of liver tissue damage.
FOS	First-order statistics: First-order statistics estimates the properties of individual pixel values. These statistics do not consider the spatial interaction that exsisits between the image pixels.
FPS	Fourier power spectrum: Texture description by means of fourier descriptors provides the means of multi-scale representation, but these descriptors lack spatial localization.
GLCM	Gray level co-occurrence matrix: Second-order statistics estimates the properties of any texture by considering the spatial interation between two pixels at a time.
GLRLM	Gray level run length matrix: Higher-order statistics estimates the properties of any texture by considering the spatial interation between a number of pixels at a time.
GWT	Gabor wavelet transform: Another method of multi-scale texture description with good spatial localization.
HCC	Hepatocellular carcinoma: The most common primary malignant focal liver lesion.
HEM	Hemangioma: The most common primary benign focal liver lesion.
Hyperechoic FLL	Hyperechoic focal liver lesion: The focal liver lesion with more echogenicity as compared to the surrounding liver parenchyma.
Hypoechoic FLL	Hypoechoic focal liver lesion: The focal liver lesion with less echogenicity as compared to the surrounding liver parenchyma.
Isoechoic FLL	Isoechoic focal liver lesion: The focal liver lesion with same echogenicity as that of the surrounding liver parenchyma.
LHCC	Large hepatocellular carcinoma: HCC lesions (>2 cm), appearance as lesion with mixed echogenicity.
Malignant FLL	Malignant focal liver lesion: Cancerous focal liver lesion.
MET	Metastasis: The most common secondary malignant focal liver lesion.
NOR	Normal liver: Normal liver has homogeneous texture with medium echogenicity (i.e., same or slightly increased echogenicity compared to the right kidney).
SHCC	Small hepatocellular carcinoma: HCC lesions (<2 cm), appearance vary from hypoechoic to hyperechoic lesions.
Typical Cyst	Typical cyst: Well-defined, round, anechoic lesion with posterior acoustic enhancement and thin imperceptible wall.
Typical FLL	Typical focal liver lesion: Focal liver lesions with classic diagnostic sonographic appearance.
Typical HEM	Typical hemangioma: Appears as a well-circumscribed uniformly hyperechoic lesion.
Typical MET	Typical metastasis: Appears with ‘target’ or ‘bull’s-eye’ appearance.

Introduction

Differential diagnosis in patients with focal liver lesions (FLLs) using B-mode ultrasound (US) images is broad due to the existence of a wide variety of sonographic appearances even with-in individual classes of FLLs [1–4]. Even then, B-mode US is the first choice for characterization of FLLs mainly due to its non-radioactive, non-invasive, inexpensive nature and real time imaging capabilities [5–7]. In comparison to B-mode US, other imaging modalities like, contrast enhanced US, contrast enhanced spiral computed tomography (CT) and magnetic resonance imaging (MRI) offer high sensitivity for characterization of FLLs, but these imaging modalities are expensive, pose greater operational inconvenience and are not widely available [1, 5, 6, 8–13]. Therefore, an efficient computer-aided classification (CAD) system for classification of FLLs based on conventional gray scale B-mode US is highly desired.

A neural network ensemble (NNE) based computer-aided diagnostic (CAD) system for commonly occurring FLLs such as Cyst, hemangioma (HEM), hepatocellular carcinoma (HCC), and metastatic carcinoma (MET) along with normal (NOR) liver tissue is proposed in this paper. A comprehensive and representative image database consisting of (1) typical and atypical cases of Cyst, HEM and MET lesions, (2) small HCC (SHCC) as well as large HCC (LHCC) lesions and (3) normal liver cases is used for classifier design.

Typical FLLs can be easily diagnosed by radiologist from their classic sonographic appearances, but differential diagnosis in the presence of atypical FLLs is considered to be a daunting challenge faced by the radiologists during routine practice [7, 9, 11, 14–17].

The sonographic appearance of normal (NOR) liver is homogeneous with slightly increased echogenicity as compared to the right kidney [18–20]. All NOR cases are considered as typical as there is no atypical appearance for NOR liver tissue. Typical Cyst appears as round, anechoic lesion with posterior acoustic enhancement and well defined thin imperceptible wall [5, 9, 10, 21]. HEM is the most common primary benign FLL [1, 7, 9, 17, 22]. Almost 70 % of all the HEM

cases encountered in routine practice are typical HEMs. Typical HEM appears as a well circumscribed uniformly hyperechoic lesion [5, 9, 10, 15, 21–23]. MET is the most common secondary malignant FLL [2, 7, 9, 21–23]. MET may occur singly or as multiple deposits of varying sizes. The typical sonographic appearance of MET lesion is the 'target' or 'bull's-eye' appearance (i.e., hypoechoic center surrounded by a hyperechoic rim) [2, 5, 7, 15, 16, 21, 22, 24]. The sample images for NOR liver and typical cases of Cyst, HEM and MET lesions are shown in Fig. 1.

Atypical Cysts appear with internal echoes and thickened irregular walls. Differential diagnosis of Cystic MET and atypical Cyst from conventional gray scale B-mode US can be quite challenging [21, 22]. Atypical HEMs are a great mimic and definite diagnosis with conventional gray scale B-mode US is difficult [9]. Atypical HEMs can be isoechoic or even hypoechoic mimicking the sonographic appearance of certain atypical metastasis [5, 7]. Atypical MET lesions can appear with extremely variable sonographic appearances ranging from anechoic, hypoechoic, isoechoic, hyperechoic and even with mixed echogenicity [5, 8–10, 23, 24]. Differentiating atypical MET lesions from HCC lesions and HEM lesions is considerably difficult [9, 11, 16, 21–23, 25].

The sample images for atypical cases of Cyst, HEM and MET lesions are shown in Fig. 2.

HCC is the most common primary malignant FLL, which occurs mostly in patients with cirrhosis [2, 5, 6, 8–10, 21, 22, 26]. In fact, in radiology practice, cirrhosis is always considered as precursor to the development of HCC. The detection of SHCCs on the top of coarse and nodular cirrhotic liver is considerably difficult [2, 9, 16, 18] accordingly, only the HCC lesions developed on cirrhotic liver are considered in this study.

Experienced participating radiologists (co-authors of this paper) opined that no sonographic appearance can be considered typical for HCC due to existence of wide variability of sonographic appearances even within SHCC and LHCC lesions. The sonographic appearances of SHCC lesions vary from hypoechoic to hyperechoic [23]. LHCC lesions appear frequently with mixed echogenicity [9, 10]. However, the participating radiologists were of the view that a representative and comprehensive dataset for designing the classifier should contain both SHCCs and LHCCs. The size of 13 SHCCs and 15 LHCCs in the acquired image database varied from 1.5 to 1.9 cm and from 2.1 to 5.6 cm, respectively. The sample images for SHCC and LHCC lesions are shown in Fig. 3.

There are certain disadvantages associated with use of conventional gray scale B-mode US for characterization of FLLs: (1) limited sensitivity for detection of small FLLs (<2 cm) developed on cirrhotic liver which is already nodular and coarse-textured [5, 8–10, 18], (2) in certain cases, sonographic appearance of HCC and atypical MET lesions are overlapping [5, 8–10, 18, 24], (3) sonographic appearances of cystic MET and atypical Cyst are often overlapping [8, 9], (4) sonographic appearances of HEM sometimes mimic HCC lesions [9, 11, 15, 17, 21–23, 26, 27] and (5) in certain cases, it is difficult to characterize isoechoic lesions with very slim liver to lesion contrast [2, 9, 15]. Thus, conventional gray scale B-mode US offers limited sensitivity for detection and characterization of FLLs [2, 5, 6, 8–10]. Therefore, it is very much desired to reduce these limitations and built an efficient CAD system with a comprehensive training dataset consisting of representative typical and atypical cases of Cyst, HEM and MET classes and both SHCC and LHCC variants of HCC image class.

The participating radiologists were of the view that the training dataset used in the present study is a comprehensive and diversified set consisting of representative images from various sub-classes.

There are very few studies in the literature for classification of FLLs. Brief details of these studies [15, 16, 21–23, 28, 29] are depicted in Table 1.

Differential diagnosis between FLLs is carried out by experienced radiologists based on sonographic features which are visually extractable. It is expected that CAD systems should yield better accuracy by using sonographic features

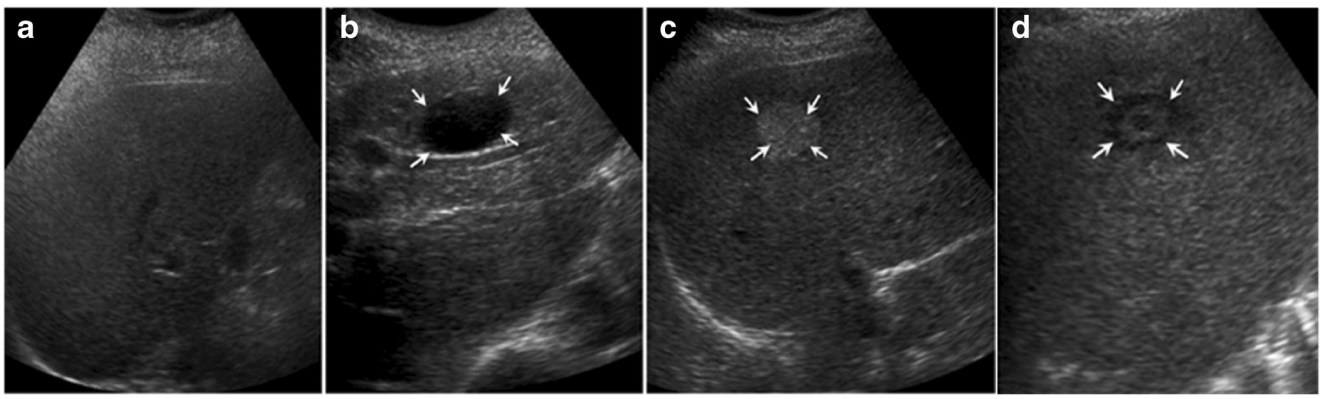

Fig. 1 Conventional gray scale B-mode liver US images. **a** Normal liver (homogeneous echotexture with medium echogenicity). **b** Typical cyst (thin walled anechoic lesion with posterior acoustic enhancement). **c** Typical HEM (well circumscribed uniformly hyperechoic appearance). **d** Typical MET ('target' or 'bull's-eye' appearance, i.e., hypoechoic center surrounded by a hyperechoic rim)

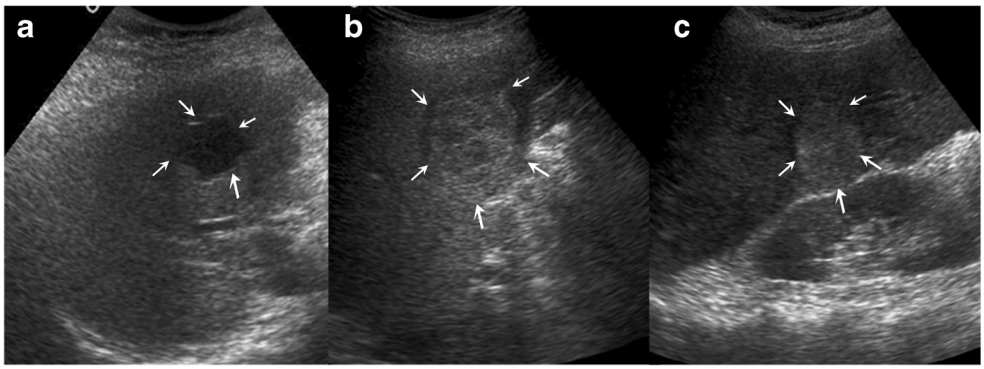

Fig. 2 Sample images for atypical cases. **a** Atypical cyst (internal echoes and irregular walls). **b** Atypical HEM (heterogeneous echotexture). **c** Atypical MET (hyperechoic, heterogeneous echotexture)

which cannot be extracted visually. These mathematical descriptors can be morphological features (based on the shape or contour of the lesion) or textural features (based on intensity distribution) [30]. Both these morphological as well as textural features are significant for developing CAD systems for breast lesions from B-mode US [31–38]. Experienced participating radiologists were of the view that morphological features does not give any significant information for characterization of FLLs from B-mode US and the same is also evident from other related researches, the proposed CAD systems for characterization of FLLs from B-mode US have relied on textural features only [15, 16, 21–23, 28, 29].

The study in [28] used first-order statistics (FOS) and gray level run length matrix (GLRLM) features for classification between NOR, HEM and malignant liver lesions by using linear discriminant analysis and neural network (NN) classifier. The study in [29] used gray level co-occurrence matrix (GLCM), autocorrelation, Laws' and edge frequency based texture features for classification of NOR, Cyst, HEM and malignant liver lesions by using a NN classifier. Their study

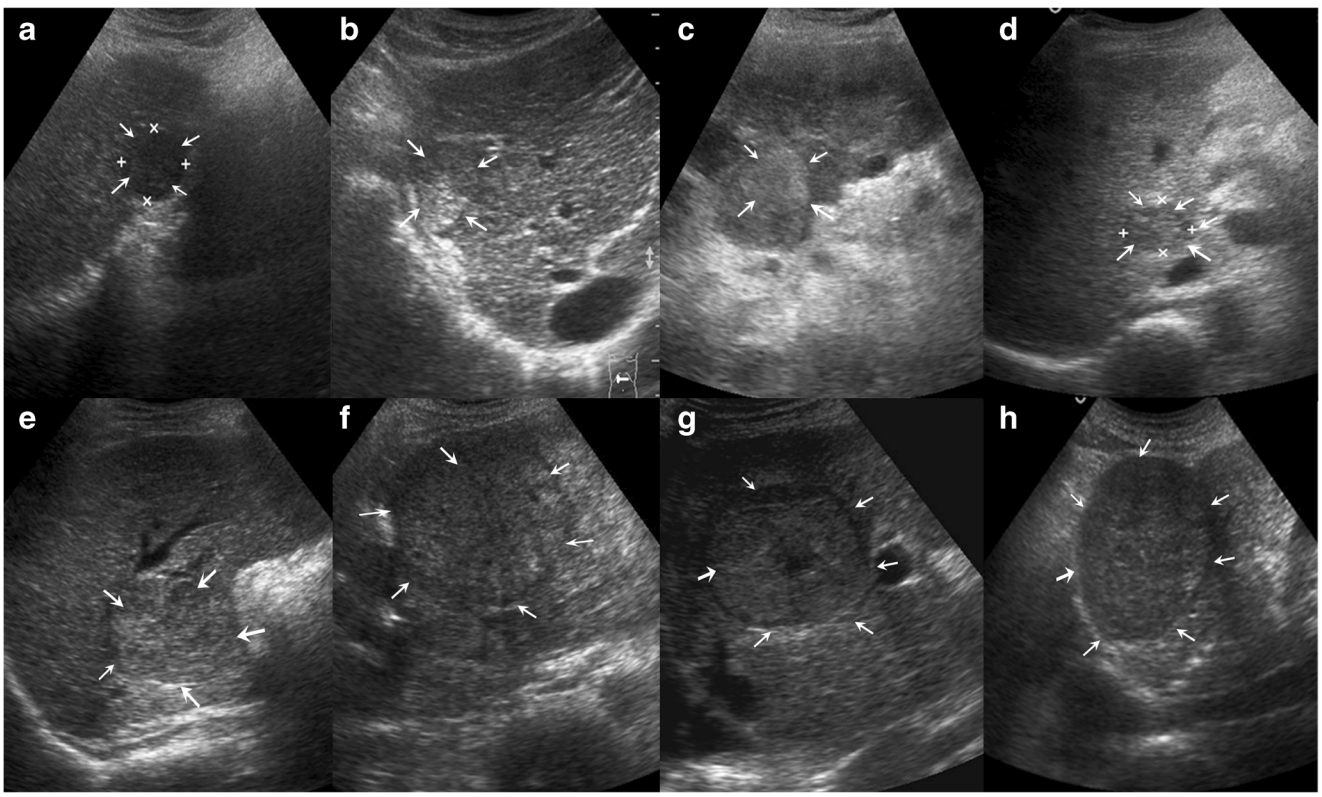

Fig. 3 Sample images for SHCC and LHCC lesions. **a** Hypoechoic SHCC. **b** Variant of SHCC with mixed echogenicity (coexistence of hyperechoic and isoechoic areas). **c** homogeneously hyperechoic SHCC **d** heterogeneously isoechoic SHCC. **e–h** Heterogeneous echotexture represents complex and chaotic structure exhibited by LHCC due to coexistence of areas of necrosis, fibrosis and active growth areas. Note: Hypoechoic halo formation is visible in **f** and **g**. Necrotic area is visible in the center of LHCC shown in **g**

Table 1 Studies on classification of FLLs

Authors (year)	Dataset description						
	Liver image classes	Patients	Images per class	No. of ROIs	ROI size (pixels)	Classifier used	Distribution of ROIs for classifier design
Sujana et al. (1996) [28]	NOR HEM Malignant	–	–	113	10×10	Neural network LDA	Training NOR (40) HEM (15), Malignant (30) Testing NOR (13) HEM (5) Malignant (10)
Yoshida et al. (2003) [23]	HEM Malignant (HCC + MET)	44	HEM (17) HCC (11) MET (16)	193	64×64	Neural network	Cross validation procedure HEM (50) HCC (87) MET (56)
Poonguzhali et al. (2007) [29]	NOR Cyst HEM Malignant	–	–	120	10×10	Neural network	Cross validation procedure NOR (30) Cyst (30) HEM (30) Malignant (30)
Mittal et al. (2011) [15]	NOR Cyst HEM HCC MET	88	NOR (16) Cyst (17) HEM (18) HCC (15) MET (45)	800	25×25	Ensemble of neural networks	Training NOR (50) Cyst (50) HEM (50) HCC (50) MET (50) Validation NOR (10) Cyst (10) HEM (10) HCC (10) MET (10) Testing NOR (172) Cyst (6) HEM (30) HCC (167) MET (125)
Virmani et al. (2013) [16]	HCC HEM	108	HCC (28) MET (32)	185	32×32	SVM	Training HCC (50) MET (50) Testing HCC (40) MET (45)
Virmani et al. (2013) [22], Yoshida et al. [23]	NOR Cyst HEM HCC MET	108	NOR (21) Cyst (12) HEM (15) HCC (28) MET (32)	491 380 IROIs*, 111 SROIs*	32×32	kNN NN PNN SVM	NOR (30) Cyst (30) HEM (40) HCC (50) MET (50) NOR (40) Cyst (25) HEM (30) HCC (40) MET (45)
Present study (2014)	NOR Cyst HEM HCC MET	108	NOR (21) Cyst (12) HEM (15) HCC (28) MET (32)	491 380 IROIs*, 111 SROIs*	32×32	Ensemble of neural networks	NOR (30) Cyst (30) HEM (40) HCC (50) MET (50) NOR (40) Cyst (25) HEM (30) HCC (40) MET (45)

SROIs are extracted to compute texture ratio features, texture features are computed from 380 IROIs. Total instances of feature vectors in the complete dataset are 380, of which 200 instances are used for training and rest 180 instances are used for testing the classifier

ROIs regions of interest, *IROIs* inside ROIs*, *SROIs* surrounding ROIs*, *SVM* Support Vector Machine, *kNN k* nearest neighbour, *PNN* probabilistic NN.

reports maximum correct classification rate of 70 % by the use of GLCM and Laws' features. In both these researches [28, 29] malignant lesions are considered as a single class; however, the diagnosis of malignant lesion as HCC or MET is clinically significant for effective treatment and management of liver malignancies [6, 9, 16]. In a recent study [16], GA-SVM based CAD system based on statistical, spectral and spatial filtering based texture features is proposed for binary classification between HCC and MET lesions.

Yoshida et al. [23] evaluated the binary classification between HEM and HCC, HEM and MET as well as HCC and MET lesions with multi-scale wavelet packet texture features and NN classifiers. Mittal et al. [15] used FOS, GLCM, GLRLM, GWT and Laws' Features

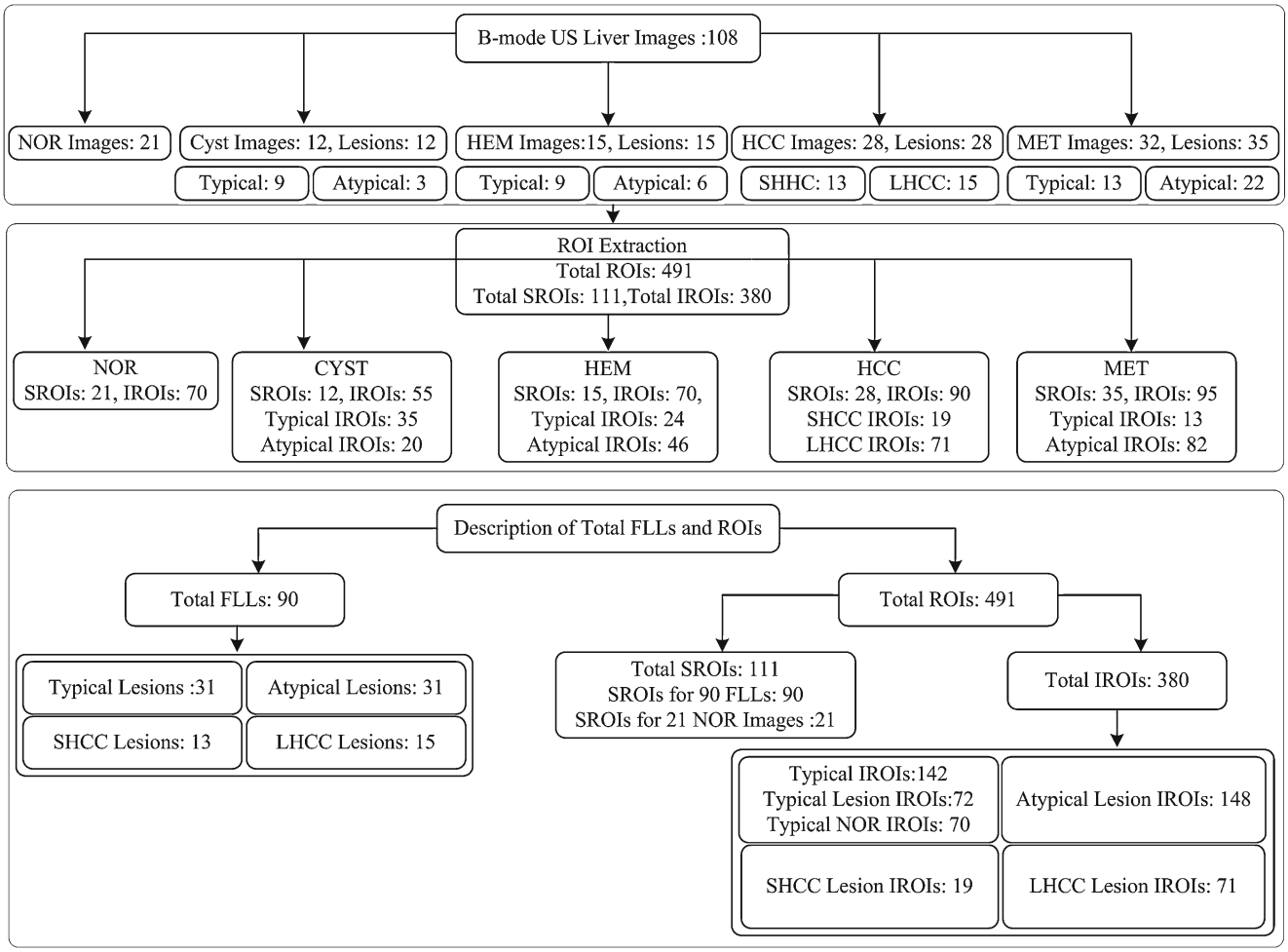

Fig. 4 Dataset description. Note: The size of SHCC lesion varied from 1.5 to 1.9 cm and size of LHCC lesion varied from 2.1 to 5.6 cm

for classification of NOR, Cyst, HEM, HCC and MET liver classes by using ensemble of NN classifiers. Virmani et al. [21, 22] reported the comparative evaluation of CAD systems for FLLs. From studies related to classification of FLLs [15, 16, 21–23, 28, 29], it is understood that statistical, spectral and spatial filtering based Laws' texture features are important for characterization of FLLs from B-mode US.

As per the best of the author's knowledge, only one study in the literature [15] has evaluated the classification between five liver image classes — Cyst, HEM, HCC, MET and NOR liver — by using a large feature vector consisting of 208 texture features extracted with statistical, spectral and spatial filtering based methods and an ensemble based CAD system. Their CAD system design with two stage classification module consisted of total 11 NNs (i.e., a single five class NN in the first stage and ten binary NNs for the second stage) obtains a good classification accuracy of 86.4 % with US images enhanced with modified anisotropic diffusion method [15]. One of the limitations of the proposed CAD by Mittal et al. [15] is that the system does not use any feature selection or feature dimensionality reduction methodology to get rid of superfluous and redundant features in a large feature set consisting of 208 texture features. Their CAD system design used the same feature set for design of primary classifier and all the ten binary NNs; however, it is worth mentioning that not all of the 208 features are necessary for the binary classification tasks. In the present work, in order to design an efficient CAD system based on ensemble of NN classifiers, feature dimensionality reduction is carried out by using principal component analysis (PCA) for designing each classifier. In several studies [15, 23, 28, 29], only ROIs within the lesions have been considered for computing texture features. Virmani et al. [16, 21, 22] used both texture and texture ratio features for classification of FLLs. These studies demonstrate that texture analysis of regions surrounding the lesion contributes towards effective characterization of HCC and MET lesions from B-Mode US images.

Typical FLLs can be easily identified by experienced radiologists by textural characteristics of regions inside the lesion but the differential diagnosis between atypical FLLs and HCCs is often carried out by observing the

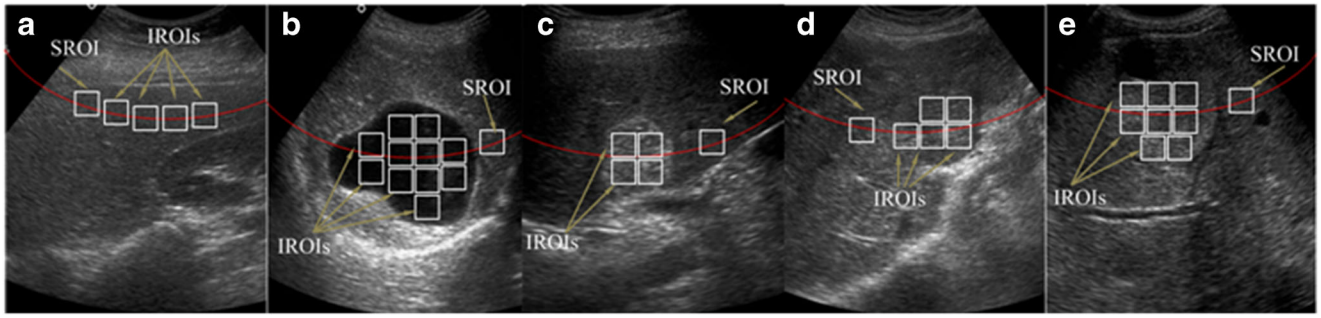

Fig. 5 **a–e** NOR, Cyst, HEM, HCC and MET image with IROIs and SROI marked. Note: For NOR image, all IROIs and SROI are taken at the same depth. A single extreme ROI is considered as SROI. For liver images with lesions, SROI is extracted from background liver parenchyma surrounding the lesion approximately at the same depth as that of the center of the lesion by avoiding inhomogeneous areas like blood vessels and liver ducts. All IROIs are regions well inside the boundary of the lesions. As shown in **e**, necrotic area within the lesions is avoided while cropping IROIs

textural characteristics of regions inside and outside of the lesion [5, 39]. The experienced participating radiologists opined that the textural analysis of regions surrounding the lesion should contribute towards effective characterization of FLLs. The present work investigates the contribution of texture information from inside and outside the lesion in characterization of FLLs from conventional gray scale B-mode US.

Materials and Methods

Materials

Dataset Description

A total of 108 B-mode liver US images were collected from the patients visiting the Department of Radiodiagnosis and Imaging, Post Graduate Institute of Medical Education and Research (PGIMER), Chandigarh, India, from March 2010 to March 2012, after obtaining informed consent from these patients for using these images for research. The medical ethics board of PGIMER, Chandigarh, granted the ethical clearance to carry out this research work. The direct digital images recorded by using Philips ATL HDI 5000 US machine equipped with multi-frequency transducer of 2–5 MHz range were used. The size of the images is 800×564 pixels with gray scale consisting of 256 tones. The display system on which the images were viewed was capable of displaying the full acquisition image matrix (i.e., it could display the 800×564 image with a 1:1 match of image pixels to display pixels).

The description of clinically acquired dataset consisting of 108 B-mode liver US images in terms of (1) distribution of these images among NOR, typical Cyst, atypical Cyst, typical HEM, atypical HEM, typical MET, atypical MET, SHCC and LHCC image sub-classes, (2) distribution of total FLLs in the dataset among typical, atypical, SHCC and LHCC lesion categories, and (3) distribution of total ROIs extracted from the dataset among SROIs and IROIs is shown in Fig. 4.

The final dataset consisting of total 111 SROIs and 380 IROIs was stored in a PC (Pentium Core 2 Duo, 2.67 GHz with 1.97 GB RAM).

Data Collection Protocols

The following protocols were followed for data collection.

(1) Experienced participating radiologists (co-authors of this paper) with 13 and 23 years of experience in US imaging ensured that all the images are of diagnostic quality (free from artifacts) and confirmed the presence of Cyst, HEM, HCC and MET lesions using liver image assessment criteria including: (a) visualization of sonographic appearances, imaging features of FLLs based on their knowledge and expertise, (b) follow-up of clinical history of the patient and other associated findings, and (c) imaging appearance on dynamic helical CT/MRI/pathological examinations and biopsy, which is an invasive procedure. (2) Only HCCs evolved on cirrhotic liver are considered. (3)The distinction between LHCC and SHCC was made by observing the size of the lesion in transverse and longitudinal views (HCC lesions less than 2 cm in size are considered SHCCs).

It must be noted that labeling of HCC lesions as SHCC or LHCC lesion and labeling of Cyst, HEM and MET lesions as typical or atypical lesion was done during data collection solely for the purpose of having representative data in the training set for designing the classifier.

Selection of Regions of Interest (ROIs)

The following protocols were followed for cropping the ROIs from the image database:

(1) The ROIs were cropped by an experienced participating radiologist by using a specially designed ROI manager software developed in Biomedical Instrumentation

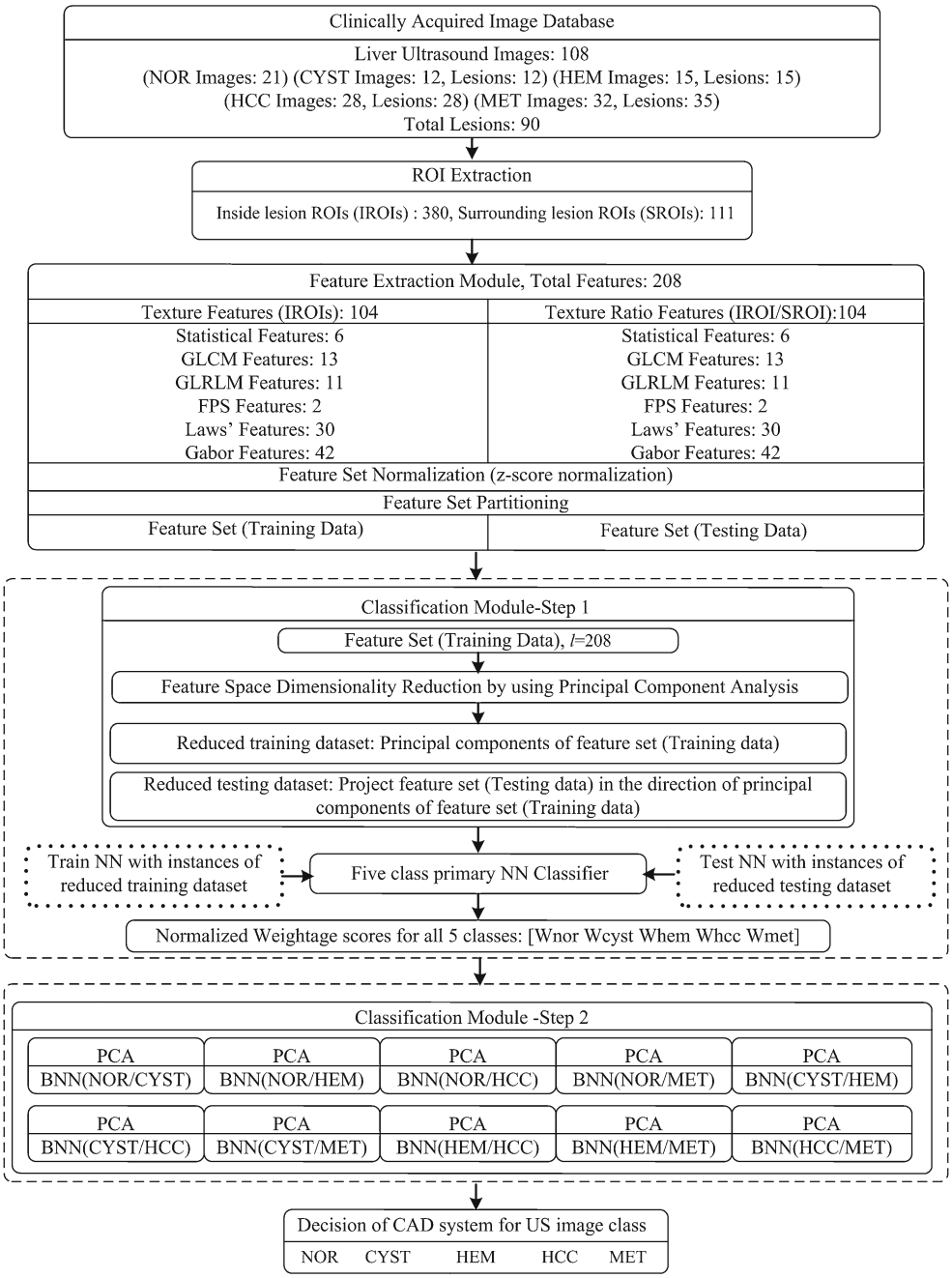

Fig. 6 Proposed NNE based CAD system for classification of FLLs from B-mode US images

Laboratory, Indian Institute of Technology, Roorkee. The ROI manager software provided the radiologist the flexibility to load the image, choose the ROI size and shape, move the ROI to any desired location over the image, freeze the ROI at any location and crop the ROIs together after the position of all the ROIs for a particular image is frozen.

(2) Two types of ROIs are used in this study, inside ROIs (IROIs) and surrounding ROIs (SROIs). For each Cyst, HEM, HCC and MET lesion maximum non-overlapping IROIs were cropped from well within the boundary of each lesion. The necrotic areas within lesions were avoided while cropping IROIs (as shown in Fig. 5e).

(3) For each lesion, a single SROI was cropped from surrounding liver parenchyma approximately at the same depth as that of the center of the lesion by avoiding the inhomogeneous structures like liver ducts and blood vessels (as shown in Fig. 5b–e).

(4) For each NOR image, a single extreme ROI is considered as SROI and all other ROIs at the same depth are considered as IROIs. SROIs and IROIs for NOR image were

Table 2 Description of texture feature vectors (TFVs)

TFVs	(*l*)
TFV1: TFV consisting of 104 texture features (6 FOS, 13 GLCM, 11 GLRLM, 2 FPS, 42 Gabor and 30 Laws' features) computed from IROIs	104
TFV2: TFV consisting of 104 texture ratio features (6 FOS, 13 GLCM, 11 GLRLM, 2 FPS, 42 Gabor and 30 Laws' features) computed by taking the ratio of texture feature computed from IROI and the corresponding SROI	104
TFV3: combined TFV consisting of 104 texture features (TFV1) and 104 texture ratio features (TFV2)	208

l length of TFV

cropped by avoiding the inhomogeneous structures like liver ducts and blood vessels (as shown in Fig. 5a).

The sample image for NOR, Cyst, HEM, HCC and MET cases from the acquired image database with ROIs marked are shown in Fig. 5.

In the present work, two types of features are considered for analysis, i.e., texture features computed from IROIs and texture ratio features computed by taking the ratio of texture feature computed from IROI and texture feature computed from the corresponding SROI.

It can be noted that the NOR liver image in Fig. 5a contains four IROIs and a corresponding SROI; thus, four instances of the texture feature set and four instances of the texture ratio feature set are obtained. Similarly, from Cyst, HEM, HCC and MET lesions shown in Fig. 5b–e, 11, four, five and eight instances of the texture feature set and 11, four, five and eight instances of the texture ratio feature set are obtained.

Selection of ROI Size

Another concern, while designing a CAD system is with the choice for the size of ROI. Mittal et al. [15] used an ROI size of 25×25 pixels while Sujana et al. [28] and Poonguzhali et al. [29] used an ROI size of 10×10 pixels for computing texture features. Virmani et al. [16, 21, 22] used an ROI size of 32×32 pixels. It is worth mentioning that the use of 10×10 pixels and even 25×25 pixels as ROI size yields a smaller number of pixels in comparison to the minimum 800 pixels required to estimate reliable statistics [16, 18, 40–42]. Yoshida et al. [23] used 64×64 pixels as ROI size, possibly because they used high-resolution scanned images instead of real US images. It is otherwise difficult to select such a large ROI size keeping in view the size of small lesions and resolution of images obtained from US machines. The ROI size of 32×32 pixels was considered appropriate for the present study to estimate reliable statistics as well as to extract maximum ROIs from the acquired image database.

Methods

Proposed NNE Based CAD System

The block diagram of proposed NNE based CAD system for classification of FLLs from B-mode US images is shown in Fig. 6.

For implementation of the proposed NNE based CAD system, the database of 380 non-overlapping IROIs and 111 SROIs was created from 108 clinically acquired B-mode US liver images. The NNE based CAD system consists of feature extraction module, and a two-step classification module. Feature space dimensionality reduction by PCA is considered as an integral part of both the steps in classification module. In feature extraction module, 104 texture features and 104 texture ratio features are computed for all 380 IROIs, resulting in feature set consisting of 380 texture feature vectors (TFVs) of length 208. The feature set is normalized using z-score normalization. The normalized feature set is bifurcated into two disjoint feature sets, i.e., feature set (training data) and feature set (testing data). PCA is carried out on the feature set (training data) and reduced training dataset of PCA derived principal components (PCs) is obtained. The reduced testing dataset is obtained by projecting the data points of the feature set (testing data) in the direction of PCs of feature set (training data). Feature space dimensionality reduction by PCA is applied individually for the design of five class NN primary classifier in step 1 of the classification module and for the design of ten mutually independent binary neural network (BNN) secondary classifiers in step 2 of the classification module in order to

Table 3 Classification performance obtained by using FS1, FS2 and FS3

Classification performance — NN classifier						
FS	OCA	ICA (NOR)	ICA (CYST)	ICA (HEM)	ICA (HCC)	ICA (MET)
FS1	66.1	77.5	92	50	37.5	77.7
FS2	75	85	76	76.6	60	75.5
FS3	82.7	87.7	92	83.3	87.5	71.1

FS feature set, *OCA* overall classification accuracy, *ICA* individual class accuracy

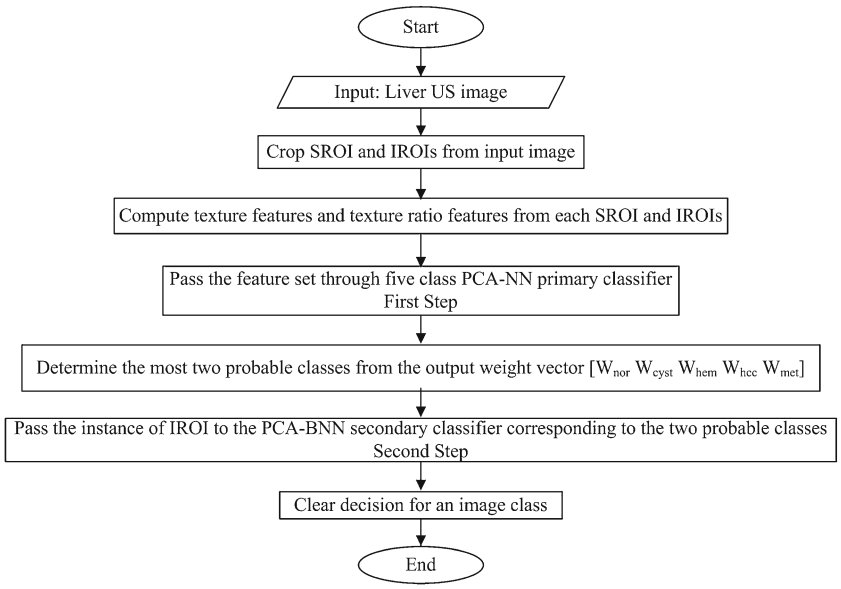

Fig. 7 Flowchart of the proposed NNE based CAD system

find out the number of PCs which could provide adequate discrimination capability in each case.

Feature Extraction Module

In the feature extraction module, initially a wide variety of visual and nonvisual sonographic features are extracted by using statistical, spectral and spatial filtering based feature extraction methods.

FOS Features A total of six FOS texture features — average gray level, standard deviation$_{FOS}$, smoothness, third moment, uniformity and entropy$_{FOS}$ — are computed for each ROI [21, 22, 43].

GLCM Features A total of 13 GLCM mean features — angular second moment, contrast, correlation, variance, inverse difference moment, sum average, sum variance, sum entropy, entropy$_{GLCM}$, difference variance, difference entropy, information measures of correlation-1, and information measures of correlation-2 are computed for each ROI [21, 22, 44–46].

GLRLM Features A total of 11 GLRLM features — i.e., short run emphasis, long run emphasis, low gray level run emphasis, high gray level run emphasis, short run low gray level emphasis, short run high gray level emphasis, long run low gray level emphasis, long run high gray level emphasis, gray level non uniformity, run length non uniformity and run percentage are computed for each ROI [21, 22, 47–49].

FPS Features Two spectral features — i.e., radial sum and angular sum of the discrete Fourier transform are computed for each ROI [21, 22, 47].

GWT Features Multi-scale features estimated at various frequency and orientations of Gabor filters provide useful description of texture [15, 21, 22, 50]. Two statistical features — mean and standard deviation are computed from the 21 filtered ROI images (Gabor outputs) obtained by using a set of Gabor wavelets at three scales and seven orientations resulting in 42 (2×3×7) texture features for each ROI.

Laws' Features Laws' features determine texture properties by performing local averaging, edge detection, spot detection, wave detection and ripple detection in texture [21, 22, 51]. Law's texture features can be computed by using special 1-D filters of lengths 3, 5, 7 and 9. Different filter lengths correspond to different resolutions for extraction of texture features from an ROI. In the present work, 1-D filters of length 5 — i.e., L5 (Level)=[1, 4, 6, 4, 1], E5 (Edge)=[−1, −2, 0, 2, 1], S5 (Spot)=[−1, 0, 2, 0, −1], W5 (Wave)=[−1, 2, 0, −2, 1] and R5 (Ripple)=[1, −4, 6, −4, 1] are used. Each of these 1-D filters is associated with the underlying microstructure of texture within the ROI image. A total of 25 2-D filters (Laws' masks) are generated by convolving these 1-D filters in a combinatorial manner [21, 22, 52, 53]. These Laws' masks are convolved with the ROI images. A 15×15 square window is applied to the resulting convolved images in order to compute texture

Table 4 Classification performance obtained by using reduced FS, i.e., FS4

NN unit	Optimal no. of PCs	OCA (%)
Five class PCA-NN based primary NN NN architecture: (I/H/O)=(6:10:5) Classes: NOR/CYST/HEM/HCC/MET	6	87.7

OCA overall classification accuracy, *I/H/O* number of neurons in Input layer/Hidden layer/Output layer

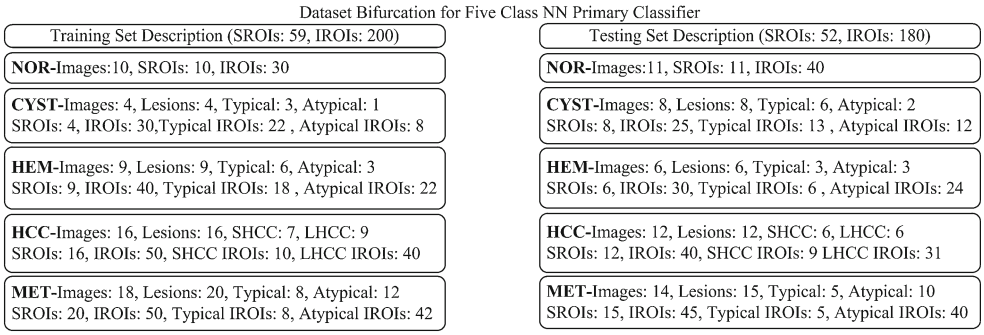

Fig. 8 The bifurcation of instances of individual classes in FS4 (training data) and FS4 (testing data) for five class PCA-NN based primary classifier

energy images (TEIs). Out of 25 Laws' masks, ten masks are identical to the other ten, if they are rotated by 90°. TEIs computed from these pairs of identical masks can be combined to obtain rotation invariant image [15, 16]. Thus, for each ROI, a total of 15 rotational invariant TEIs are obtained. Two statistics (i.e., mean and standard deviations) are computed for each rotational invariant TEIs resulting in 30 (15×2) texture features for each ROI.

For detection and characterization of FLLs initially, three TFVs are computed using FOS, GLCM, GLRLM, FPS, GWT and Laws' texture feature extraction methods. The brief description of these TFVs is tabulated in Table 2.

Initially, all the three feature sets, i.e., FS1, FS2 and FS3, consisting of instances of TFV1, TFV2 and TFV3, respectively, as described in Table 2 are used for classification of FLLs from B-mode US images. The FS3 consisting of instances of combined TFV (i.e., TFV3) was considered for analysis, to investigate the effect of including texture information from SROIs in differential diagnosis between FLLs from B-mode US. The classification experiments are carried out by using NN classifiers. The classification performance with respect to overall classification accuracy (OCA) values and the individual class accuracy (ICA) values obtained with FS1, FS2 and FS3 is summarized in Table 3.

In Table 3, it can be observed that FS3 yield highest classification accuracy in comparison to FS1 and FS2 which justifies the premise that both texture features and texture ratio features contribute for effective characterization of FLLs from B-mode US. Thus FS3, consisting of combined TFVs is considered for all further analysis.

Classification Module

The proposed NNE based CAD system incorporates two steps in classification module. The first step of the classification module consists of a single five class NN classifier and the second step of the classification module consists of ten BNN classifiers.

The FS3 consisting of instances of combined TFV of length 208, i.e., TFV3, is used for the present classification task. This combined TFV may contain redundant and correlated features, which if used for classifier design can degrade its performance in terms of accuracy and reliability. Thus, PCA is used for feature space dimensionality reduction before classifier design in both the steps of classification module. The PCA algorithm ensures that the covariance of any of the components with any other component is zero. As it is quite possible that the PCs accounting for a lesser amount of variance in the data may be significant for the classification task, and also since the computed PCs are uncorrelated to each other, it is always reasonable to step through the first few PCs for building the classification model [21, 22, 54, 55]. In the present work, the optimal number of PCs to be retained for classification task is determined empirically by repeated experiments carried out by stepping through first 15 PCs to build the classification models.

The flow chart showing the working of proposed NNE based CAD system is shown in Fig. 7.

Classification Module (Step 1) The first step of classification module consists of a single five class PCA-NN based primary classifier. As shown in Table 3, the FS3 consisting of instances of combined TFV (i.e., TFV3) yields higher OCA in comparison with FS2 and FS1. Thus, FS3 is subjected to feature space dimensionality reduction using PCA. The number of PCs yielding the maximum OCA are retained in reduced feature set (FS4) for classifier design. It is observed that the first six PCs yields maximum OCA of 87.7 %. Thus, reduced features set, i.e., FS4 consisting of instances of reduced TFVs of length 6 (optimal number of PCs), is used for the design of the five class PCA-NN based primary classifier [22]. The classification performance obtained by FS4 is shown in Table 4 [22].

For design of each PCA-NN based primary classifier, the optimal number of neurons in the hidden layer is obtained by trial-and-error procedure. Experiments were carried out with different numbers of hidden neurons and it was observed that for ten neurons in hidden layer a reasonable tradeoff between accuracy and convergence is obtained [15, 21, 22].

The bifurcation of instances of individual classes in FS4 (training data) and FS4 (testing data) in case of five class PCA-NN based primary classifier is shown is shown in Fig. 8.

The five class PCA-NN based primary classifier yields weightage scores for five liver image classes. Normalization of this five-dimensional output weight vector makes it analogous to probability outputs for each class. The prediction of output weight vector [Wnor Wcyst Whem Whcc Wmet] for all the 180 TFVs in the FS4 (testing data) is stored for analysis.

Classification Module (Step 2) The second step of classification module consists of ten mutually independent PCA-BNN based secondary classifiers for NOR/Cyst, NOR/HEM, NOR/

Fig. 9 The bifurcation of instances of individual classes in feature set (training data) and feature set (testing data) for ten PCA-BNN based secondary classifiers

Table 5 Optimal number of PCs and resulting overall classification accuracy for ten PCA-BNN secondary classifiers

NN unit	Optimal number of PCs	OCA (%)
PCA-BNN1:(2:4:2)-NOR/CYST	2	100
PCA-BNN2:(2:4:2)-NOR/HEM	2	100
PCA-BNN3:(6:4:2) -NOR/HCC	6	98.7
PCA-BNN4:(5:4:2)- NOR/MET	5	96.4
PCA-BNN5:(2:4:2)-CYST/HEM	2	100
PCA-BNN6:(2:4:2)-CYST/HCC	2	98.4
PCA-BNN7:(2:4:2)-CYST/MET	2	95.7
PCA-BNN8:(2:4:2)- HEM/HCC	2	98.5
PCA-BNN9:(3:4:2)-HEM/MET	3	92.0
PCA-BNN10:(2:4:5)–HCC/MET	3	97.6

HCC, NOR/MET, Cyst/HEM, Cyst/HCC, Cyst/MET, HEM/HCC, HEM/MET and HCC/MET classes, respectively. The output weight vector predicted by five class PCA-NN based primary classifier for an unknown test instance in FS4 (testing data) is used to determine the first two most probable classes, based on which it is directed to the corresponding binary PCA-NN based secondary classifier for crisp classification between two classes. The proposed approach can be understood as analogous to first querying about the diagnosis of an unknown test case with an experienced radiologist with expertise of providing interpretation among all the five liver image classes and based on his advice on first two most probable classes again querying another expert radiologist which specializes in interpretation of these two most probable classes only. It is expected that the overall result will improve by including the second step.

The bifurcation of instances of individual classes in feature set (training data) and feature set (testing data) in the case of ten PCA-BNN secondary classifiers is shown is shown in Fig. 9.

The optimal number of PCs and the resulting OCA for all ten PCA-BNN based secondary classifiers is reported in Table 5.

For designing each PCA-BNN secondary classifier, the optimal number of neurons in the hidden layer is obtained by trial-and-error procedure. After repeated experimentation with different numbers of hidden neurons it was observed that with four neurons in hidden layer a reasonable tradeoff between accuracy and convergence is obtained. The output of the neuron corresponding to the labeled class is set to 1 and the output of other neurons is set to 0. The learning of the network is supervised and back propagation algorithm with adaptive learning rate and momentum is used to obtain the desired input–output relationship [15].

Table 6 Experiments carried out in the present study

Experiments carried out in the present study	
Experiment no. 1	To obtain Classification performance of five class PCA-NN based primary, i.e., output of first step of the classification module
Experiment no. 2	To obtain Classification performance of Proposed NNE based CAD system, i.e., output of second step of the classification module

Results

The brief details of the experiments carried out in this study are given in Table 6.

Results (Experiment 1)

The classification performance obtained by the five class PCA-NN based primary classifier, i.e., step 1 of classification module, is reported in Table 7.

Table 7 shows that out of a total of 180 testing instances, 22 instances are MIs and remaining 158 testing instances are correctly classified instances. Thus, first step of the classification module yields the OCA of 87.7 % (158/180). It can be noted that 158 out of 180 correctly classified instances consisted of 33 (out of 40) NOR cases, 24 (out of 25) Cyst cases, 28 (out of 30) HEM cases, 36 (out of 40) HCC cases and 37 (out of 45) MET cases. Thus, the first step of classification module yields ICA values of 82.5 % (33/40), 96 % (24/25), 93.3 % (28/30), 90 % (36/40) and 82.2 % (37/45) for NOR, Cyst, HEM, HCC and MET cases, respectively [22].

It can be observed that the 22 misclassified instances (MIs) out of a total of 180 testing instances consisted of seven (out of 40) NOR cases, one (out of 25) Cyst case(s), two (out of 30) HEM cases, four (out of 40) HCC cases and eight (out of 45) MET cases.

Furthermore, it is observed that, from a total of 22 MIs, 17 MIs have the second highest probability for the correct class and the remaining five MIs have the third highest probability for the correct class.

The 17 (out of 22) MIs for which the second probability is for the correct class, consisted of seven (out of seven) misclassified NOR cases, one (out of one) misclassified Cyst case, two (out of two) misclassified HEM cases, three (out of four) misclassified HCC cases and four (out of eight) misclassified MET cases, respectively.

The five (from a total of 22) MIs for which the third probability is for the correct class consisted of zero (out of seven) misclassified NOR cases, zero (out of one) misclassified Cyst case, zero (out of two) misclassified HEM cases, one (out of four) misclassified HCC cases and four (out of eight) misclassified MET cases, respectively. These five MIs are peculiar MIs, as it is observed that for all these instances, there is a slim difference between the predicted probability values for all classes and even the highest probability value representing the

Table 7 Classification performance obtained by the five class PCA-NN based primary classifier (Step 1)

Classification performance: five class PCA-NN based primary classifier								
NN arch.	CM						OCA (%)	ICA (%)
6:10:5		NOR	CYST	HEM	HCC	MET	87.7	
	NOR	33	0	2	4	1		ICA (NOR): 82.5
	CYST	0	24	0	0	1		ICA (CYST): 96.0
	HEM	1	0	28	0	1		ICA (HEM): 93.3
	HCC	1	2	0	36	1		ICA (HCC): 90.0
	MET	1	0	4	3	37		ICA (MET): 82.2

CM confusion matrix, *OCA* overall classification accuracy, *ICA* individual class accuracy

predicted class is less than 0.4. This signifies that these peculiar MIs are confusing cases, as PCA-NN based primary classifier has assigned a low weightage for all the classes for these cases. Furthermore, it is noteworthy that these peculiar MIs are observed only for HCC and MET cases.

The prediction of five class PCA-NN based primary classifier for first two most probable classes in 180 instances of feature set (testing data) is given in Table 8.

In Table 8, it can be noticed that out of 180 instances in the feature set (testing data), there is not even a single instance with CYST and HEM among the first two most probable classes. This is in agreement with the fact that there is no overlap between sonographic appearances of Cyst and HEM image classes. Associated radiologists opined that while atypical Cyst can overlap significantly with cystic metastasis cases but there is no overlap even between atypical cases of Cyst and HEM image classes.

Results (Experiment 2)

In experiment 2, the TFVs corresponding to testing instances described in Table 8 are fed to corresponding PCA-BNN based secondary classifiers and the results obtained are reported in Table 9.

Table 8 Prediction of the first two most probable classes by five class PCA-NN primary classifier for 180 testing instances of the feature set (testing data)

Class pair	Testing instances (TIs)	Class pair	Testing instances (TIs)
NOR/CYST	7	CYST/HCC	22
NOR/HEM	12	CYST/MET	17
NOR/HCC	38	HEM/HCC	8
NOR/MET	20	HEM/MET	37
CYST/HEM	Nil	HCC/MET	19

TIs=7, for class pair NOR/CYST indicates that for seven of 180 testing instances, the first highest and the second highest probability predictions of PCA-NN based primary classifier is among NOR or Cyst classes; therefore, these seven testing instances will be directed to PCA-BNN based secondary classifier for NOR/CYST cases

Table 9 shows that out of the total 180 testing instances, nine instances are MIs and remaining 171 testing instances are correctly classified instances. Thus, the second step of the classification module yields the OCA of 95 % (171/180). It can be noted that the 171 (out of 180) correctly classified instances consisted of 40 (out of 40) NOR cases, 24 (out of 25) Cyst cases, 29 (out of 30) HEM cases, 38 (out of 40) HCC cases and 40 (out of 45) MET cases. Thus, second step of classification module yields ICA values of 100 % (40/40), 96 % (24/25), 96.6 % (29/30), 95 % (38/40) and 88.8 % (40/45) for NOR, Cyst, HEM, HCC and MET cases, respectively.

It is interesting to note that the first step of the classification module yielded 22 (out of 180) MIs and by incorporating the second step of the classification module, the number of MIs is reduced to 9 (out of 180).

Furthermore, it is observed that the 17 (out of 22) MIs predicted by the first step of classification module, for which the second highest probability was for the correct class, 14 (out of 17) cases are correctly classified by the second step of the classification module and the remaining (3/17) remained misclassified. The five (out of 22) peculiar MIs, as predicted by the first step of the classification module, remained misclassified after the second step also. This is expected as for these cases the third highest probability prediction is for the correct class, so these cases were not directed to the correct BNNs in the second step of classification module. It can be visualized that 1HEM** correctly classified as HEM by the first step is misclassified as MET by the second step.

The classification performance obtained by the proposed NNE based CAD system is summarized in Table 10.

It can be observed that by including the second step in the classification module, the number of MIs has decreased from 22 (out of 180) to 9 (out of 180); thus, the OCA has increased from 87.7 % to 95 %.

However, it is worth mentioning that as for five (out of nine) peculiar MIs, the PCA-NN based primary classifier (first step of the classification module) has assigned a low weightage for all the classes (the highest probability being

Table 9 Description of misclassified instances (MIs) predicted by secondary PCA-BNN based classifiers for 180 instances of the feature set (testing data)

BNN	Testing instances	Misclassified instances
NOR/CYST	7 (2 NOR, 5 CYST)	2 NOR and 5 Cyst correctly classified, MIs=0
NOR/HEM	12 (4 NOR, 7 HEM, 1 MET*)	4 NOR and 7 HEM correctly classified, MIs=1 [One *peculiar case** of MET misclassified as NOR by first step remains misclassified as NOR by second step]
NOR/HCC	38 (21 NOR, 16 HCC, 1 MET*)	21 NOR and 16 HCC correctly classified, MIs=1 [One *peculiar case** of MET misclassified as HCC by first step is misclassified as NOR by second step]
NOR/MET	20 (13 NOR, 6 MET, 1 HCC*)	13 NOR and 6 MET correctly classified, MIs=1 [One *peculiar case** of HCC misclassified as NOR by first step remains misclassified as NOR by second step]
CYST/HEM	Nil	Nil
CYST/HCC	22 (14 Cyst, 7 HCC, 1 MET*)	14 CYST and7HCC correctly classified, MIs=1 [One *peculiar case** of MET misclassified as HCC by first step remains misclassified as HCC by second step]
CYST/MET	17 (6 CYST, 11 MET)	5 CYST and 11 MET correctly classified, MIs=1 [One case of Cyst misclassified as MET by first step remains misclassified as MET (atypical cyst resembling cystic metastasis]
HEM/HCC	8 (1 HEM, 6 HCC, 1 MET*)	1 HEM and 6 HCC predicted correctly, MIs=1 [One *peculiar case** of MET misclassified as HEM by first step is misclassified as HCC by second step]
HEM/MET	37 (22 HEM, 15 MET)	21 HEM and 14 MET correctly classified, MIs=2 [One case of MET misclassified as HEM by first step remains misclassified as HEM by second step (atypical cyst resembling cystic metastasis)] [1 HEM correctly classified as HEM by first step is misclassified as MET by second step]**
HCC/MET	19 (10 HCC, 9 MET)	9 HCCand 9 MET correctly classified, MIs=1 [One case of HCC misclassified as MET by first step remains misclassified as MET by second step]

MIs misclassified instances, *TIs* testing instances; total TIs=180, total MIs=9. Note: Out of total 9 MIs, 5 are peculiar cases* for which the PCA-NN based primary classifier has assigned a low weightage for all classes, i.e. the highest weightage assigned to the most probable class is 0.4 and also there is very small difference between weightages assigned to the other classes. One MI** correctly classified by first step is missclassified by the second step.

0.4). The developed CAD system is an interactive system which displays the weightage [Wnor Wcyst Whem Whcc Wmet], i.e., probability outputs yielded by PCA-NN based primary classifier for each test instance. Therefore, for peculiar MIs having a low highest weightage and slim difference between all class weightages, it is expected that the radiologist should consider an alternative approach for confirming the diagnosis, which may be taking a second opinion from another expert, patient's history, other imaging modalities, biopsy, etc.

Table 10 Classification performance of proposed NNE based CAD system

Classification performance: NNE based CAD system							
CM						OCA	ICA
	NOR	CYST	HEM	HCC	MET	95.0	
NOR	40	0	0	0	0		ICA (NOR): 100
CYST	0	24	0	0	1		ICA (CYST): 96.0
HEM	0	0	29	0	1		ICA (HEM): 96.6
HCC	1	0	0	38	1		ICA (HCC): 95.0
MET	2	0	1	2	40		ICA (MET): 88.8

CM confusion matrix, *OCA* overall classification accuracy, *ICA* individual class accuracy

Analysis of Misclassified Instances

The analysis of MIs predicted by the five class PCA-NN based primary classifier (i.e., after the first step of the classification module) and of MIs predicted by the proposed NNE based CAD system (i.e., after the second step of the classification module) in terms of various sub-classes is reported is reported in Table 11.

Table 11 shows that by incorporating step 2 of the classification module, the ICA values for NOR, atypical HEM,

Table 11 Analysis of 22 (out of 180) misclassified instances predicted by five class PCA-NN based primary classifier and nine (out of 180) misclassified instances predicted by proposed NNE based CAD system

S. no.	Five class PCA-NN based primary classifier	Proposed NNE based CAD system
1.	NOR cases: (40)	NOR cases: (40)
	MIs: 7 ICA (NOR): 82.5 %	MIs: Nil ICA (NOR): 100 %
2.	Typical Cyst cases: (13)	Typical Cyst cases: (13)
	MIs: Nil ICA (Typical Cyst): 100 %	MIs: Nil ICA (Typical Cyst): 100 %
3.	Atypical Cyst cases: (12)	Atypical Cyst cases: (12)
	MIs: 1 ICA (Atypical Cyst): 91.6 %	MIs: 1 ICA (Atypical Cyst): 91.6 %
4.	Typical HEM cases: (6)	Typical HEM cases: (6)
	MIs: Nil ICA (Typical HEM): 100 %	MIs: 1 ICA (Typical HEM): 83.3 %
5.	Atypical HEM cases: (24)	Atypical HEM cases: (24)
	MIs: 2 ICA (Atypical HEM): 91.6 %	MIs: Nil ICA (Atypical HEM): 100 %
6.	Small HCC cases: (9)	Small HCC cases: (9)
	MIs: Nil ICA (SHCC): 100 %	MIs: Nil ICA (SHCC): 100 %
7.	Large HCC cases: (31)	Large HCC cases: (31)
	MIs: 4 ICA (LHCC): 87 %	MIs: 2 ICA (LHCC): 93.5 %
8.	Typical MET cases: (5)	Typical MET cases: (5)
	MIs: 2 ICA (Typical MET): 60 %	MIs: 2 ICA (Typical MET): 60 %
9.	Atypical MET cases: 40	Atypical MET cases: (40)
	MIs: 6 ICA (Atypical MET): 85 %	MIs: 3 ICA (Atypical MET): 92.5 %
10.	Total Typical cases: (64)[a]	Total Typical cases: (64)[a]
	MIs: 9 ICA (Typical Cases): 85.9 %	MIs: 3 ICA (Typical Cases): 95.3 %
11.	Total Atypical cases: (76)[b]	Total Atypical cases: (76)[b]
	MIs: 9 ICA (Atypical Cases): 88.1 %	MIs: 6 ICA (Atypical Cases): 92.1 %

MIs misclassified instances, *ICA* individual class accuracy

[a] Total typical cases in testing dataset=40 NOR+13 CYST+6 HEM+5 MET=64

[b] Total atypical cases in testing dataset =12 CYST+24 HEM+40 MET= 76

Large HCC and atypical MET cases have increased from 82.5 %, 91.6 %, 87 % and 85 % to 100 %, 100 %, 93.5 % and 92.5 %, respectively. The ICA values for typical cyst, atypical cyst, small HCC and typical METs have remained the same, i.e., 100 %, 91.6 %, 100 % and 60 %, respectively. However, it can be visualized that ICA for typical HEM cases has decreased from 100 % to 83.3 %. It is expected that ICA for typical HEM cases should increase by adding more cases for classifier design. Overall, by incorporating the second step of the proposed classification module the ICA values for typical and atypical cases has increased from 85.9 % and 88.1 % to 95.3 % and 92.1 %, respectively. Given this fact, conventional gray scale B-mode US has limited sensitivity for detection and characterization of atypical cases of FLLs, the performance obtained by the proposed NNE based CAD system is encouraging.

In Tables 7 and 10, it can be observed that the ICA values for HCC and MET cases have increased from 90 % and 82.2 % to 95 % and 88.8 %, respectively. These results indicate that the proposed NNE based CAD system can facilitate better management of focal liver malignancies by providing second opinion in case of highly overlapping sonographic appearances of HCC and MET lesions.

Conclusion

From the experiments carried out in the present study, it is observed that significant improvement in classification performance is obtained by including the texture ratio features along with texture features computed from IROIs for characterization of FLLs from B-mode US. Thus, it can be concluded that the texture analysis of the region surrounding the lesion significantly contribute towards the differential diagnosis of FLLs using B-mode US images. Further, it is worth mentioning that by application of PCA to feature set consisting of 208 texture features (104 texture features and 104 texture ratio features); the information required for the classification of FLLs was squeezed in the first six PCs. It is concluded that by incorporating the second step of classification module the OCA value increases from 87.7 % to 95 % and ICA values for typical and atypical cases increase from 85.9 % and 88.1 % to 95.3 % and 92.1 %, respectively. The promising results obtained by the proposed CAD system with such a diversified, comprehensive and representative dataset used in the present study indicate that the proposed NNE based CAD system can be routinely used in clinical environment to assist radiologists in lesion interpretation and differential diagnosis of FLLs using conventional B-mode gray scale US images.

Acknowledgements The author Jitendra Virmani would like to acknowledge Ministry of Human Resource Development (MHRD), India for financial support. The authors wish to acknowledge the Department of Electronics and Communication Engineering, Jaypee University of Information Technology, Waknaghat, Himachal Pardesh, India, the Department of Electrical Engineering, Indian Institute of Technology, Roorkee, India and Department of Radiodiagnosis and Imaging, Postgraduate Institute of Medical Education and Research, Chandigarh, India for their constant patronage and support in carrying out this research work. The authors would like to thank the anonymous reviewers for their substantive and informed review, which led to significant improvements in the manuscript.

References

1. Namasivayam S, Salman K, Mittal PK, Martin D, Small WC: Hypervascular hepatic focal lesions: spectrum of imaging features. Curr Probl Diagn Radiol 36(3):107–123, 2007
2. Tiferes DA, D'lppolito G: Liver neoplasms: imaging characterization. Radiol Bras 41(2):119–127, 2008
3. Wernecke K, Vassallo P: The distinction between benign and malignant liver tumors on sonography: value of a hypoechoic halo. Am J Radiol 159:1005–1009, 1992
4. Mittelstaedt CA: Ultrasound as a useful imaging modality for tumor detection and staging. Cancer Res 1980(40):3072–3078, 1980
5. Bates J: Abdominal Ultrasound How Why and When, 2nd edition. Churchill Livingstone, Oxford, 2004, pp 80–107
6. Soye JA, Mullan CP, Porter S, Beattie H, Barltrop AH, Nelson WM: The use of contrast-enhanced ultrasound in the characterization of focal liver lesions. Ulster Med J 76(1):22–25, 2007
7. Pen JH, Pelckmans PA, Van Maercke YM, Degryse HR, De Schepper AM: Clinical significance of focal echogenic liver lesions. Gastrointest Radiol 11(1):61–66, 1986
8. Colombo M, Ronchi G: Focal Liver Lesions—Detection, Characterization, Ablation. Springer, Berlin, 2005, pp 167–177
9. Harding J, Callaway M: Ultrasound of focal liver lesions. Rad Mag 36(424):33–34, 2010
10. Jeffery RB, Ralls PW: Sonography of Abdomen. Raven, New York, 1995
11. Tsurusaki M, Kawasaki R, Yamaguchi M, Sugimoto K, Fukumoto T, Ku Y, Sugimura K: Atypical hemangioma mimicking hepatocellular carcinoma with a special note on radiological and pathological findings. Jpn J Radiol 27(3):156–160, 2009
12. Sandulescu L, Saftoiu A, Dumitrescu D, Ciurea T: Real-time contrast-enhanced and real-time virtual sonography in the assessment of benign liver lesions. J Gastrointest Liver Dis 17(4):475–478, 2008
13. Nielsen MB, Bang N: Contrast enhanced ultrasound in liver imaging. Eur J Radiol 51:S3–S8, 2004
14. Marsh JI, Gibney RG, Li DKB: Hepatic hemangioma the presence of fatty infiltration: an atypical sonographic appearance. Gastrointest Radiol 14:262–264, 1989
15. Mittal D, Kumar V, Saxena SC, Khandelwal N, Kalra N: Neural network based focal liver lesion diagnosis using ultrasound images. Int J Comput Med Imaging Graph 35(4):315–323, 2011
16. Virmani J, Kumar V, Kalra N, Khandelwal N: Characterization of primary and secondary malignant liver lesions from B-mode ultrasound. J Digit Imaging 26(6):1058–1070, 2013
17. Vilgrain V, Boulos L, Vullierme MP, Denys A, Terris B, Menu Y: Imaging of atypical hemangiomas of the liver with pathologic correlation. Radiographics 20(2):379–397, 2000
18. Virmani J, Kumar V, Kalra N, Khandelwal N: SVM-based characterization of liver ultrasound images using wavelet packet texture descriptors. J Digit Imaging 26(3):530–543, 2013
19. Minhas F, Sabih D, Hussain M: Automated classification of liver disorders using ultrasound images. J Med Syst 36(5):3163–3172, 2011
20. Virmani J, Kumar V, Kalra N, Khandelwal N: Prediction of liver cirrhosis based on multiresolution texture descriptors from B-mode ultrasound. Int J Converg Comput 1(1):19–37, 2013
21. Virmani J, Kumar V, Kalra N, Khandelwal N: PCA-SVM based CAD system for focal liver lesions from B-mode ultrasound. Def Sci J 63(5):478–486, 2013
22. Virmani J, Kumar V, Kalra N, Khandelwal N: A comparative study of computer-aided classification systems for focal hepatic lesions from B-mode ultrasound. J Med Eng Technol 37(4):292–306, 2013
23. Yoshida H, Casalino DD, Keserci B, Coskun A, Ozturk O, Savranlar A: Wavelet packet based texture analysis for differentiation between benign and malignant liver tumors in ultrasound images. Phys Med Biol 48:3735–3753, 2003
24. Scheible W, Gossink BB, Leopold G: Gray scale echo graphic patterns of hepatic metastatic disease. Am J Roentgenol 129:983–987, 1977
25. Albrecht T, Hohmann J, Oldenburg A, Wolf K: Detection and characterisation of liver metastases. Eur Radiol Suppl 14(S8):25–P33, 2004
26. Di Martino M, De Filippis G, De Santis A, Geiger D, Del Monte M, Lombardo CV, Rossi M, Corradini SG, Mennini G, Catalano C: Hepatocellular carcinoma in cirrhotic patients: prospective comparison of US, CT and MR imaging. Eur Radiol 23(4):887–896, 2013
27. Kimura Y, Fukada R, Katagiri S, Matsuda Y: Evaluation of hyperechoic liver tumors in MHTS. J Med Syst 17(3/4):127–132, 1993
28. Sujana S, Swarnamani S, Suresh S: Application of artificial neural networks for the classification of liver lesions by image texture parameters. Ultrasound Med Biol 22(9):1177–1181, 1996
29. Poonguzhali S, Deepalakshmi, Ravindran G: Optimal feature selection and automatic classification of abnormal masses in ultrasound liver images. In: Proceedings of IEEE International Conference on Signal Processing, Communications and Networking, ICSCN'07, 503–506, 2007
30. Kim SH, Lee JM, Kim KG, Kim JH, Lee JY, Han JK, Choi BI: Computer-aided image analysis of focal hepatic lesions in ultrasonography: preliminary results. Abdom Imaging 34(2):183–191, 2009
31. Huang YL, Wang KL, Chen DR: Diagnosis of breast tumors with ultrasonic texture analysis using support vector machines. Neural Comput Appl 15:164–169, 2006
32. Nandi RJ, Nandi AK, Rangayyan RM, Scutt D: Classification of breast masses in mammograms using genetic programming and feature selection. Med Biol Eng Comput 44(8):683–694, 2006
33. Diao XF, Zhang XY, Wang TF, Chen SP, Yang Y, Zhong L: Highly sensitive computer aided diagnosis system for breast tumor based on color Doppler flow images. J Med Syst 35(5):801–809, 2011
34. Moayedi F, Azimifar Z, Boostani R, Katebi S: Contourlet based mammography mass classification. In: Proceedings of ICIAR 2007. LNCS 4633:923–934, 2007
35. Alto H, Rangayyan R: An indexed atlas of digital mammograms for computer-aided diagnosis of breast cancer. Ann Telecommun 58: 820–835, 2003
36. Huang YL, Chen DR, Jiang YR, Kuo J, Wu HK, Moon WK: Computer-aided diagnosis using morphological features for classifying breast lesions on ultrasound. Ultrasound Obstet Gynecol 32:565–572, 2008
37. André T, Rangayyan R: Classification of breast masses in mammograms using neural networks with shape, edge sharpness, and texture features. J Electron Imaging 15(01):684481, 2006
38. Rangayyan RM, Nguyen TM: Pattern classification of breast masses via fractal analysis of their contours. Int Congr Ser 1281:1041–1046, 2005
39. Lee WL, Hsieh KS, Chen YC: A study of ultrasonic liver images classification with artificial neural networks based on fractal geometry and multiresolution analysis. Biomed Eng Appl Basis Commun 16(2):59–67, 2004
40. Badawi AM, Derbala AS, Youssef ABM: Fuzzy logic algorithm for quantitative tissue characterization of diffuse liver diseases from ultrasound images. Int J Med Inform 55:135–147, 1999
41. Fukunaga K: Introduction to Statistical Pattern Recognition. Academic, New York, 1990
42. Kadah YM, Farag AA, Zurada JM, Badawi AM, Youssef AM: Classification algorithms for quantitative tissue characterization of diffuse liver disease from ultrasound images. IEEE Trans Med Imaging 15(4):466–478, 1996
43. Virmani J, Kumar V, Kalra N, Khandelwal N: A rapid approach for prediction of liver cirrhosis based on first order statistics. In:

Proceedings of IEEE International Conference on Multimedia, Signal Processing and Communication Technologies, IMPACT-2011, 212–215, 2011
44. Haralick R, Shanmugam K, Dinstein I: Textural features for image classification. IEEE Trans Syst Man Cybern SMC-3(6):610–121, 1973
45. Virmani J, Kumar V, Kalra N, Khandelwal N: Prediction of cirrhosis based on singular value decomposition of gray level cooccurrence matrix and a neural network classifier. In: Proceedings of IEEE International Conference on Developments in E-systems Engineering, DeSe-2011, 146–151, 2011
46. Virmani J, Kumar V, Kalra N, Khandelwal N: SVM-based characterisation of liver cirrhosis by singular value decomposition of GLCM matrix. Int J Artif Intell Soft Comput 4(1):276–296, 2013
47. Galloway RMM: Texture analysis using gray level run lengths. Comput Graph Image Process 4:172–179, 1975
48. Chu A, Sehgal CM, Greenleaf JF: Use of gray value distribution of run lengths for texture analysis. Pattern Recogn Lett 11:415–420, 1990
49. Dasarathy BV, Holder EB: Image characterizations based on joint gray level-run length distributions. Pattern Recogn Lett 12:497–502, 1991
50. Lee C, Chen S H: Gabor wavelets and SVM classifier for liver diseases classification from CT images. In: Proceedings of IEEE International Conference on Systems, Man, and Cybernetics, 548–552, 2006
51. Laws KI: Rapid texture identification. SPIE Proc Semin Image Process Missile Guid 238:376–380, 1980
52. Sharma M, Markou M, Singh S: Evaluation of texture methods for image analysis. In: Proceedings of the Seventh Australian and New Zealand Intelligent Information Systems Conference, 117–121, 2001
53. Virmani J, Kumar V, Kalra N, Khandelwal N: Prediction of cirrhosis from liver ultrasound B-mode images based on Laws' masks analysis. In: Proceedings of IEEE International Conference on Image Information Processing, ICIIP-2011, 1–5, 2011
54. Kadir A, Nugroho LE, Susanto A, Santosa PI: Performance improvement of leaf identification system using principal component analysis. Int J Adv Sci Technol 44:113–124, 2012
55. Du C, Linker R, Shaviv A: Identification of agricultural Mediterranean soils using mid-infrared photoacoustic spectroscopy. Geoderma 143(1–2):85–90, 2008